

Linear System Models for Ultrasonic Imaging: Application to Signal Statistics

Roger J. Zemp, Craig K. Abbey, and Michael F. Insana

Abstract—Linear equations for modeling echo signals from shift-variant systems forming ultrasonic B-mode, Doppler, and strain images are analyzed and extended. The approach is based on a solution to the homogeneous wave equation for random inhomogeneous media. When the system is shift-variant, the spatial sensitivity function—defined as a spatial weighting function that determines the scattering volume for a fixed point of time—has advantages over the point-spread function traditionally used to analyze ultrasound systems. Spatial sensitivity functions are necessary for determining statistical moments in the context of rigorous image quality assessment, and they are time-reversed copies of point-spread functions for shift variant systems. A criterion is proposed to assess the validity of a local shift-invariance assumption. The analysis reveals realistic situations in which in-phase signals are correlated to the corresponding quadrature signals, which has strong implications for assessing lesion detectability. Also revealed is an opportunity to enhance near- and far-field spatial resolution by matched filtering unfocused beams. The analysis connects several well-known approaches to modeling ultrasonic echo signals.

I. INTRODUCTION

THE objective assessment of image quality in medical imaging systems is a topic of growing importance. Our ability to rigorously quantify the performance of clinically relevant tasks, such as identification of low-contrast lesions, can help us improve diagnostic performance and may influence standards of practice. Information theoretic approaches to performance assessment may help us understand fundamental limits of ultrasound systems, quantify information content of signals, and reveal optimum strategies for image processing. A key element of ultrasonic performance assessment is the computation of echo-signal covariance matrices that define likelihood functions. Current probabilistic models are valid only near the transducer focal region and in dense random media of point scatterers [1], [2]. These models further assume the impulse response function is shift-invariant. Motivation for our work stems from the need to extend existing statistical models to more realistic shift-variant imaging systems and nonstationary random scattering media.

Manuscript received May 31, 2002; accepted December 9, 2002. This work was supported in part by the National Institutes of Health, R01 CA 82497.

The authors are with the Department of Biomedical Engineering, University of California, Davis CA 95616 (e-mail: mfinsana@ucdavis.edu).

Pulse-echo imaging may be described as a linear system that obeys the imaging equation:

$$g(\mathbf{t}) = \int dx h(\mathbf{x}, \mathbf{t}) \gamma(\mathbf{x}) + n(\mathbf{t}) = \mathcal{H}\{\gamma(\mathbf{x})\} + n(\mathbf{t}), \quad (1)$$

where g is the radio-frequency (RF) echo signal consisting of a set of A-scan lines. The function h is the pulse-echo spatio-temporal impulse response, which is generally shift variant. \mathcal{H} is the linear operator associated with h . γ is called the object function (often stochastic), and n is signal-independent zero-mean additive Gaussian noise. A vector \mathbf{t} , representing, for example, the axial and lateral (temporal) dimensions of the echo data, will span the data space (see Appendix A for details). Points in object space, in contrast, are positioned according to the spatial vector $\mathbf{x} = (x_1, x_2, x_3)$. The dimensionality of the domain of h is the dimensionality of the object space plus that of the data space. Thus, for a single A-scan line, h is a four-dimensional (4-D) function: one dimension of time and three of space. Eq. (1) describes how spatial variations in physical properties of the object that interacts with the sound waves are mapped into data. It will describe acoustic transmission and reception (including the effects of diffraction, attenuation, and scattering), electromechanical coupling of the transducer, and electronic processing. It is a linear system in the sense that $\mathcal{H}\{a\gamma_1 + b\gamma_2\} = a\mathcal{H}\{\gamma_1\} + b\mathcal{H}\{\gamma_2\}$ for any object functions γ_1 and γ_2 , and for any constants a and b . Thus, (1) assumes linearity in the system electronics, in the scattering response, and in acoustic propagation.¹ Partial motivation for writing the imaging equation in form (1) is the immediate connection to literature on objective assessment of image quality [3]–[5].

Investigators frequently use linear systems approaches in ultrasound research, some of which will be reviewed here. The imaging equation (1) is a generalization of many such approaches in the literature. Tupholme [6] and Stepanishen [7]–[10] were among the first to model ultrasonic imaging systems using the impulse response approach; the system impulse response was viewed as a series of convolutions of various impulse response functions representing acoustic, electromechanical, and scattering influences. This description led to a representation of a linear

¹Nonlinear propagation in transmission could be allowable in (1) because scattering in soft tissue is very weak and propagation back to the transducer may be described as linear. The model for a tissue harmonic imaging system would be linear in the object function, but not in the driving voltage.

system, in which the object function was studied one point scatterer at a time. Other researchers have considered γ as a continuum variable that depends on perturbations in density and compressibility [11], [12].

Jensen [13] developed a linear model for the propagation and scattering of ultrasound in tissue based on a time-dependent Green's function solution to the wave equation in heterogeneous media. This is similar to our time-independent Green's function approach. However, he expresses the imaging equation (1) in terms of a spatial convolution [13, equation 45] and ignores attenuation and noise. Our results reduce to his with a shift-invariance assumption, an attenuation-free medium, and no noise. Moreover, we take the extra step to apply the linear system theory to signal statistics.

Walker and Trahey [14] present a k -space linear systems model of ultrasound systems that they use to calculate speckle variance and image correlations. Their application of the Fraunhofer approximation limits the results to the focal and far field regions. Walker [15] extends his results to shift-variant systems, but does not make an important distinction between point-spread and spatial sensitivity functions. Our results provide a rigorous underpinning to the computation of spatially varying statistics. Walker and Trahey [14] suggest that wavefront phase curvature does not contribute to speckle correlations. This conclusion was conditioned upon some assumptions that will be elucidated in Section VII. We demonstrate situations in which wavefront curvature can indeed be quite important in the evaluation of speckle texture.

Our aim is to demonstrate how the imaging equation (1) provides a comprehensive representation of shift-variant systems applied to continuous scattering media. Our motivation is to form a bridge between ultrasound physics and the statistical image quality assessment literature. The approach uses a solution of the homogenous wave equation in inhomogeneous media. We relate our model to existing theory and show that it is well suited for evaluation of the statistical properties of ultrasound signals and images.

II. RADIO-FREQUENCY SIGNALS

Assume that the imaging medium is heterogeneous in density ρ and compressibility κ on a scale smaller than the wavelength, although the average density ρ_o , average bulk compressibility κ_o , and speed of sound, $c = 1/\sqrt{\rho_o\kappa_o}$ are approximately constant macroscopically throughout the medium. With the small amplitude approximation, acoustic propagation is well described by the homogeneous wave equation for inhomogeneous media [16]–[18],

$$\nabla \cdot \left(\frac{1}{\rho(\mathbf{x})} \nabla p(\mathbf{x}, t) \right) - \kappa(\mathbf{x}) \frac{\partial^2 p(\mathbf{x}, t)}{\partial t^2} = 0, \quad (2)$$

where $p(\mathbf{x}, t)$ is the pressure field. Here time is a scalar quantity representing pulse-echo time for a single A-scan line. Taken from the classic acoustics literature [19], Insana and Brown [18] provide a time-independent solution

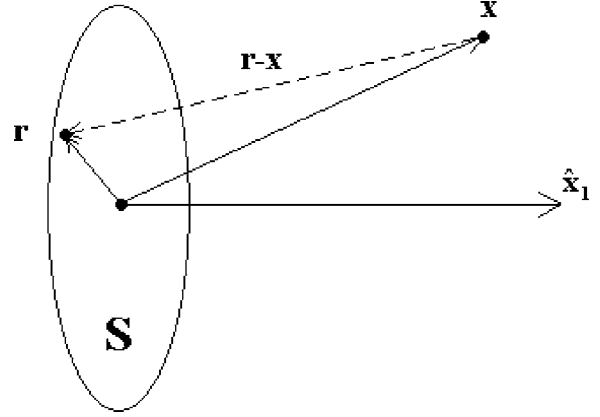


Fig. 1. Illustration of the measurement geometry. Field and observation points are labeled \mathbf{x} and \mathbf{r} , respectively.

to (2) using a weak scattering Green's function approach. In particular, they give an expression for the pressure scattered to observation points \mathbf{r} from a distributed scattering media. We will base our linear systems model on their approach, and connect it to linear systems approaches presented by other investigators.

Backscattered energy at frequency ω propagates to the transducer aperture where it is coherently summed to generate a net instantaneous force, $f_\omega(t)$. Using the plane-impedance approximation $p = \rho_o c u$ relating pressure p to particle velocity u normal to the detector surface S , and integrating over S , we obtain [20]:

$$f_\omega(t) = \frac{1}{2} i \rho_o c k U(\omega) \exp(i\omega t) \int_V d\mathbf{x} \left\{ k^2 \left(\frac{\Delta\kappa(\mathbf{x})}{\kappa_o} \right) A^2(\mathbf{x}, k) + \left(\frac{\Delta\rho(\mathbf{x})}{\rho(\mathbf{x})} \nabla A(\mathbf{x}, k) \cdot \nabla A(\mathbf{x}, k) \right) \right\}. \quad (3)$$

Eq. (3) is described in Appendix B. Here $\Delta\kappa$ and $\Delta\rho$ are spatial fluctuations in κ and ρ about their respective means, $U(\omega)$ is the transducer surface velocity amplitude on transmission,

$$A(\mathbf{x}, k) \equiv \frac{1}{2\pi} \int_S dS \xi(\mathbf{r}) \frac{\exp(-ik|\mathbf{r} - \mathbf{x}|)}{|\mathbf{r} - \mathbf{x}|} = 2 \int_S dS \xi(\mathbf{r}) G(\mathbf{r} | \mathbf{x}), \quad (4)$$

is the velocity potential due to a unit amplitude sinusoidal excitation [17], ξ is the transducer apodization function, which may be complex to allow for focusing, and $G(\mathbf{r} | \mathbf{x})$ in (4) is the Green's function that describes the propagation of scattered waves created at field point \mathbf{x} to observation points \mathbf{r} on the transducer surface, as labeled in Fig. 1. Note that an assumption of separability between apodization (transducer geometry) and the driving velocity is made. The magnitude of the wave-vector \mathbf{k} can be complex to allow for attenuation; for local plane waves

$k = \omega/c - i\alpha(\omega)$, where α is the frequency dependent attenuation coefficient. The middle expression in (4) is the well-known Rayleigh integral [21], representing a linear superposition of excitations from elements of the transducer surface.² Eq. (3) shows that scattering occurs at locations in the object of density and compressibility variations. The pattern of scattered sound is different for these two types of perturbations because density variations interact with the spatial gradient of the acoustic field A while compressibility variations interact with the field itself. Two copies of the field weightings A and ∇A are required to represent transmission and reception.

A weighted superposition of forces at each frequency in the transmitted pulse gives the measured echo-signal voltage (neglecting noise):

$$g(t) = \int d\omega Y(\omega) f_\omega(t). \quad (5)$$

$Y(\omega)$ is the complex electromechanical coupling coefficient of the transducer. Neglecting noise, (3) and (5) may be considered one form of linear system (1) operating on perturbations in density and compressibility. A more useful form of (5) may be obtained if one considers field points that are a distance greater than the aperture dimension³ [22] or media where perturbations in density contribute negligibly to the scattered field. In such cases, the pulse-echo spatiotemporal impulse response in (1) may be defined from (5) as:

$$h(\mathbf{x}, t) = \int d\omega Y(\omega) \left[\frac{1}{2} i \rho_o c k U(\omega) \right] k^2 A^2(\mathbf{x}, k) \exp(i\omega t), \quad (6)$$

and the object function γ in (1) represented as:

$$\gamma(\mathbf{x}) \equiv \left(\frac{\Delta\kappa(\mathbf{x})}{\kappa_o} - \frac{\Delta\rho(\mathbf{x})}{\rho(\mathbf{x})} \right) \cong -2 \frac{\Delta z(\mathbf{x})}{z_o}. \quad (7)$$

For local plane waves, $z(\mathbf{x}) = \sqrt{\rho(\mathbf{x})/\kappa(\mathbf{x})}$ is the acoustic impedance, z_o is the mean impedance, and $\Delta z(\mathbf{x}) = z(\mathbf{x}) - z_o$. The last expression in (7) holds only for small perturbations in density and compressibility. Eq. (6) is an impulse response in the sense that it describes the response of the system to a point scatterer (a delta function in space). Pulsed excitation is incorporated by the superposition of frequency components initiated at transmission and filtered by the system.

It is a straightforward exercise to show that (6) and (7) can be used to represent (1) in the time domain in terms of convolutions. The electromechanical impulse response is indicated by h_y . In the absence of dispersive attenuation, the transmit impulse response (which, by the principle of reciprocity is the same as the receive impulse response)

is the velocity potential due to a temporal delta function excitation:

$$\begin{aligned} h_a(\mathbf{x}, t) &= \frac{1}{2\pi} \int_S dS \xi(\mathbf{r}) \frac{\delta(t - |\mathbf{r} - \mathbf{x}|/c)}{|\mathbf{r} - \mathbf{x}|} \\ &= \mathfrak{F}_t^{-1} \{ A(\mathbf{x}, k) \}. \end{aligned} \quad (8)$$

Consequently, the echo signal may be expressed as:

$$\begin{aligned} g(t) &= \int_V d\mathbf{x} \left[\left\{ h_y(t) * u(t) * \left(\frac{\partial}{\partial t} h_a(t, \mathbf{x}) \right) \right. \right. \\ &\quad \left. \left. * h_a(t, \mathbf{x}) \right\} * s(t, \mathbf{x}) \right] + n(t). \end{aligned} \quad (9)$$

Here the convolutions are over the time variable, u is the surface velocity, and s is the scattering response such that $s(t, \mathbf{x}) = \mathfrak{F}_t^{-1} \{ \gamma(\mathbf{x}) k^2(\omega) \}$, where \mathfrak{F}_t^{-1} is the inverse temporal Fourier transform operator. From the properties of convolutions, the temporal derivative can be moved to act upon any of the other functions. If the transmit and receive apertures are not the same, (9) should involve both transmit and receive impulse response functions. With s taken as a point scatterer, and neglecting the k^2 filtering action of scattering, a form of (9) was derived with a different approach by Tupholme [6] and Stepanishen [7]–[9] and is the basis of a number of simulation packages and papers on linear systems.

The spatiotemporal impulse response (6) may be written in terms of convolutions:

$$\begin{aligned} h(\mathbf{x}, t) &= -\frac{1}{c^2} \frac{\partial^2}{\partial t^2} \\ &\quad \left\{ h_y(t) * h_y(t) * v(t) * \frac{\partial}{\partial t} h_a(\mathbf{x}, t) * h_a(\mathbf{x}, t) \right\}, \end{aligned} \quad (10)$$

where the surface velocity has been written as a convolution $u(t) = h_y(t) * v(t)$ between the transducer electromechanical impulse response and the driving voltage. Note that the driving voltage need not be an impulse to call h an impulse response function. It is an impulse response in the sense that a spatial impulse $\gamma(\mathbf{x}) = \delta(\mathbf{x} - \mathbf{x}_o)$ gives a noise-averaged linear response $h(\mathbf{x}_o, t)$. Also note that although (3)–(6) allow for dispersive attenuation (in contrast to existing theory [6]–[10], [13]) by allowing a complex wave-vector, (8)–(10) do not, although one could easily add a plane-wave type of attenuation by convolving (10) in time with a position-dependent, pulse-echo attenuation filter. A practical alternative to the time-domain impulse response technique for evaluating (3)–(6) computationally is the spatial-frequency domain angular spectrum method [21], [23] that includes direction-dependent attenuation.

Like others [11]–[13] our approach describes a spatially distributed scattering function as a continuous distribution of point scatterers, and it attaches physical meaning to s by connecting it to variations in density and compressibility. Contrary to (9), in (6) and (10) we choose to couple the k^2 filtering action of scattering (object properties) with acoustic and electromechanical impulse response

²The Rayleigh integral is valid only for planar or quasiplanar surfaces. For curved surfaces, a cosine directionality term should be included in the integral, as described by the Rayleigh-Sommerfeld diffraction formula [21].

³The approximation made is $\nabla A(\mathbf{x}, k) \cdot \nabla A(\mathbf{x}, k) = -k^2 A^2(\mathbf{x}, k)$ for points $x > r_{\max}$, where r_{\max} is the radius of the aperture.

functions (system properties). It should be clear that there is some flexibility in defining which factors are associated with the object and which with the system. That decision depends on the application.

III. POINT-SPREAD AND SPATIAL SENSITIVITY FUNCTIONS

As discussed in Appendix A, we may consider the data space variable \mathbf{t} to be a vector representing, for example, the axial and lateral dimensions of a B-mode image. With this interpretation, various samples in the data may be the result of different spatiotemporal, impulse-response functions, i.e., shift variance.

Imaging systems are often studied using point-spread functions. An ultrasonic point-spread function (psf) is obtained from an ensemble of echoes recorded from one stationary point scatterer. The psf is a data-space slice through the higher dimensional impulse response $h(\mathbf{x}, \mathbf{t})$. Point-spread functions characterize spatial resolution. Consider the psf representing noisy RF data from a point scatterer fixed at location \mathbf{x}_0 :

$$\begin{aligned} \text{psf}_{x_0}(\mathbf{t}) &= \left\langle \int d\mathbf{x} h(\mathbf{x}, \mathbf{t}) \delta(\mathbf{x} - \mathbf{x}_0) + n(\mathbf{t}) \right\rangle_n \\ &= \int d\mathbf{x} h(\mathbf{x}, \mathbf{t}) \delta(\mathbf{x} - \mathbf{x}_0) = h(\mathbf{t} | \mathbf{x}_0). \end{aligned} \quad (11)$$

Here, the notation $\langle \rangle_n$ represents an ensemble average⁴ over noise variations in the stochastic quantity n . When the noise level is sufficiently low, averaging can be neglected. The spatiotemporal impulse response h at time \mathbf{t} and position \mathbf{x}_0 is equivalent to the point-spread function at sample time \mathbf{t} obtained when scanning a point source at position \mathbf{x}_0 .

Shown in Figs. 2(a)–(c) are RF data matrices illustrating the psfs $g(t_1, t_2) = h(t_2, t_1 | \mathbf{x}_0)$ generated using Field II [24] by scanning a point scatterer placed at three different positions in the field of a linear array transducer: near field, focal zone, and far field. Fig. 2 was formed by pulsing and receiving along a number of parallel lateral A-scan lines. With this scanning configuration, at any given depth, the point-spread function is conveniently shift-invariant in the lateral (vertical) direction. At first glance, the curvature of the psf wavefronts may seem counterintuitive. One might expect, for example, a transmitted wavefront to be concave in the near field because concave focusing is being used. Convex near-field curvature is observed because the pulse-echo transit time is smaller when a (concave) transducer's edge is nearer in pulse-echo transit time to the point scatterer than when the scatterer is centered with respect to the transducer. Also note that the phase oscillations in the psf maintain a constant frequency along each A-scan line. This is why the width of the psf in the

direction normal to the wavefront seems to narrow at the edges. The low magnitude X-shape components in the psf are focusing flaws and include edge waves [25].

Of significance for modeling signal statistics is the spatial distribution of h for a fixed time [i.e., $h(\mathbf{x} | \mathbf{t})$, which we refer to as the spatial sensitivity function (ssf)]. This is to be contrasted with the psf that describes temporal rather than spatial variation. The ssf is an object-space slice through $h(\mathbf{x}, \mathbf{t})$ that describes how the impulse response for a fixed-measurement time changes as the point scatterer is moved in space. An alternative perspective is that, for each data sample, the ssf describes how sensitive the imaging system is to point scatterer positions located throughout the object. Figs. 2(d)–(f) display spatial sensitivity functions corresponding to near-field, focal region, and far-field pulse-echo times. They were obtained by generating a sequence of psfs: $\{h(\mathbf{t} | \mathbf{x}), h(\mathbf{t} | \mathbf{x} + \Delta\mathbf{x}), \dots, h(\mathbf{t} | \mathbf{x} + N\Delta\mathbf{x})\}$, where $\Delta\mathbf{x}$ represents an increment in the axial direction. Each psf was sampled along a particular pulse-echo axial time point \mathbf{t} , and the resulting lateral scan vectors corresponding to each incremental position were assembled into a spatial sensitivity image. It should be emphasized that, for a given temporal point in data space, an ssf is a 3-D function of space, and we are only displaying a 2-D slice through this distribution. The dimensionality of the psf depends on the dimensionality of the data space: for 2-D imaging the psf will be 2-D and for 3-D imaging the psf will be 3-D.

Spatial sensitivity functions are essential for studying first- and second-order moments of samples or pairs of samples in the data set. For example, to study the covariance between samples recorded at \mathbf{t} and \mathbf{t}' , and modeling the object function as a zero-mean, unit-variance, white Gaussian random variable, we need to compute:

$$\begin{aligned} \langle g(\mathbf{t})g(\mathbf{t}') \rangle_{n,\gamma} &= \iint d\mathbf{x}d\mathbf{x}' \langle \gamma(\mathbf{x})\gamma(\mathbf{x}') \rangle_\gamma h(\mathbf{x} | \mathbf{t})h(\mathbf{x}' | \mathbf{t}') \\ &\quad + \langle n(\mathbf{t})n(\mathbf{t}') \rangle_n \\ &= \int d\mathbf{x} h(\mathbf{x} | \mathbf{t})h(\mathbf{x} | \mathbf{t}') + \sigma_n^2 \delta(\mathbf{t} - \mathbf{t}'), \end{aligned} \quad (12)$$

which requires spatial sensitivity functions. Techniques for calculating statistical moments for shift-invariant and shift-variant systems were presented previously [15], but these contributions presumed the point-spread function as the critical quantity. In Section VI, we emphasize that a local shift-invariance approximation is needed to use point-spread functions in place of sensitivity functions.

IV. IN-PHASE AND QUADRATURE SIGNALS

The in-phase (I) and quadrature (Q) decomposition allows a single A-scan echo signal to be represented by:

$$\begin{aligned} g(t) &= g_I(t) \cos(\omega_0 t) - g_Q(t) \sin(\omega_0 t) \\ &= \text{Re} \{ \exp(i\omega_0 t) [g_I(t) + ig_Q(t)] \}. \end{aligned} \quad (13)$$

The quantity in curly brackets is the analytic signal $g(t) + i\tilde{g}(t)$, where the tilde represents the Hilbert trans-

⁴By ensemble average we mean $\langle f \rangle_n \equiv \int f(n)pdf(n)dn$, where pdf is the probability density of n .

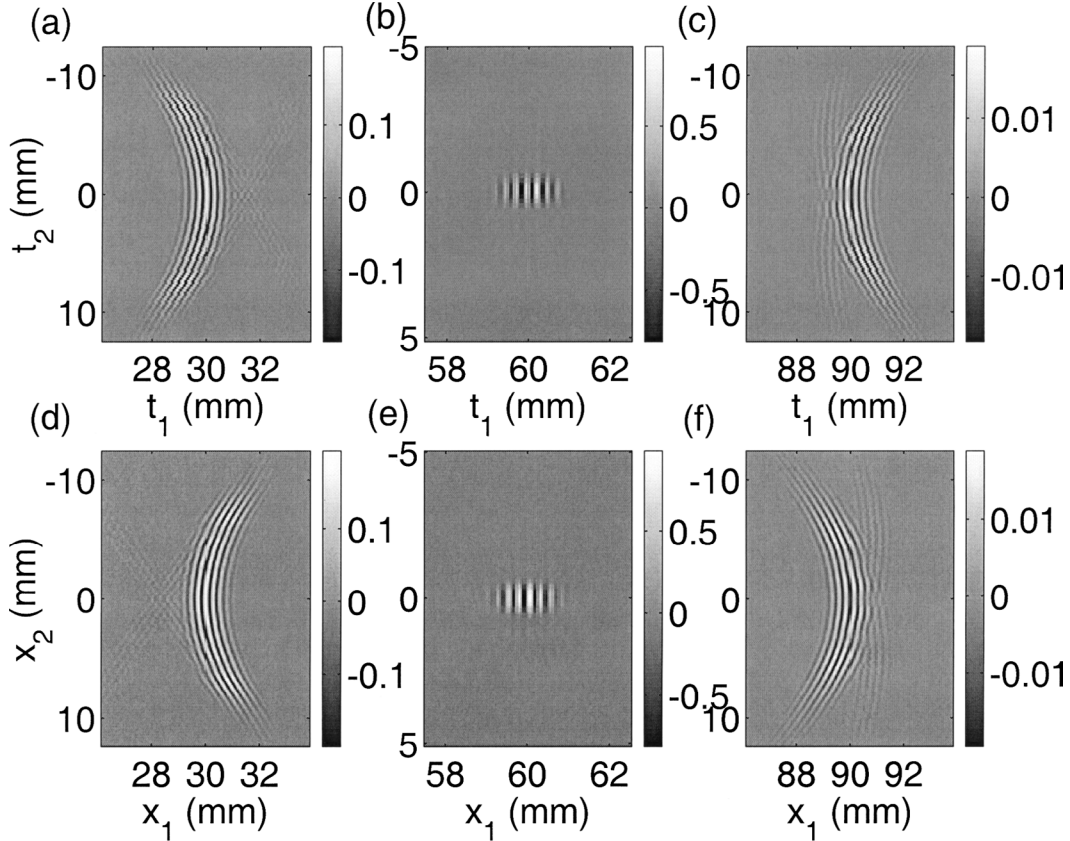


Fig. 2. Point-spread (a)–(c) and spatial sensitivity (d)–(e) functions for a 3 MHz array transducer. Images of psfs represent spread from one scatterer positioned at 30 (near field), 60 (focal region), and 90 mm (far field), respectively. Similarly, spatial sensitivity functions are shown for pulse-echo temporal intervals corresponding to times labeled by half the pulse-echo path distance: 30, 60, and 90 mm, respectively. The psf and ssf functions were normalized by the maximal focal region magnitude. Also, the axes for the psf images here and in subsequent figures are plotted in millimeters for convenience in comparing with the ssfs. The array consisted of 64 active elements of width one wavelength, height 5 mm, and interelement gap separation of 0.1 mm. The electronic focus of the array was 60 mm. The excitation was taken as a four cycle pulse filtered by the aperture electromechanical response simulated as a four-cycle Hanning-windowed pulse. The psf images were generated with Field II, then filtered to include the effects of attenuation and scattering. The medium was taken to have sound speed of 1540 m/s, and attenuation coefficient of 0.3 dB/cm/MHz^{1.1}. The ssfs were generated from an ensemble of psfs as described above.

form. Because in-phase and quadrature components g_I and g_Q are baseband signals, they can typically be sampled at a much lower rate than the RF echo signal. This representation saves data transfer and computational times while preserving information content in the signal. Because of its common use, it is desirable to model the $[I, Q]$ decomposition with a linear systems approach. To this end, the echo signal may be written as:

$$\begin{aligned} g(t) &= \int d\mathbf{x} \gamma(\mathbf{x}) e^{i\omega_o t} \mathfrak{S}_t^{-1} \{H(\omega - \omega_o | \mathbf{x})\} + n(t) \\ &= \exp(i\omega_o t) \int d\mathbf{x} \gamma(\mathbf{x}) h_o(\mathbf{x}, t) + n(t), \end{aligned} \quad (14)$$

where H is the frequency response of h , and h_o is the demodulated spatiotemporal impulse response, in general complex. The in-phase and quadrature components of an echo signal thus may be modeled from (1) as:

$$\begin{aligned} g_I(t) &= \int d\mathbf{x} \gamma(\mathbf{x}) h_I(\mathbf{x}, t) + n_I(t), \\ g_Q(t) &= \int d\mathbf{x} \gamma(\mathbf{x}) h_Q(\mathbf{x}, t) + n_Q(t). \end{aligned} \quad (15)$$

Here n_I and n_Q are assumed to be independent Gaussian noise processes. The functions h_I and h_Q are the real and imaginary parts of h_o , and will be referred to as in-phase and quadrature spatiotemporal impulse response functions, respectively. Shown in Fig. 3 are the images of h_I and h_Q , visualized in the spatial and temporal domains—or in other words, the in-phase and quadrature point-spread and spatial sensitivity functions. Note that the I and Q psfs Figs. (a) and (b) contain no axial phase oscillations, as these temporal variations have been demodulated. The lateral banded pattern occurs because of the pulse-echo wavefront curvature. A changing temporal axial phase thus shifts energy between the in-phase and quadrature channels. The I and Q ssfs of Figs. 3(c) and (d) are markedly different than the I and Q psfs in that the former exhibit axial spatial phase ($\exp(ikx)$) oscillations. The in-phase and quadrature ssfs are 90° out of phase and, therefore, those echo signals are uncorrelated.

By replacing $h(\mathbf{x} | \mathbf{t})$ with $h_I(\mathbf{x} | \mathbf{t})$ in (12), the covariance of the in-phase signal at times \mathbf{t} and \mathbf{t}' may be computed. Current theory, valid only in the focal region, suggests that the statistical properties of fully developed

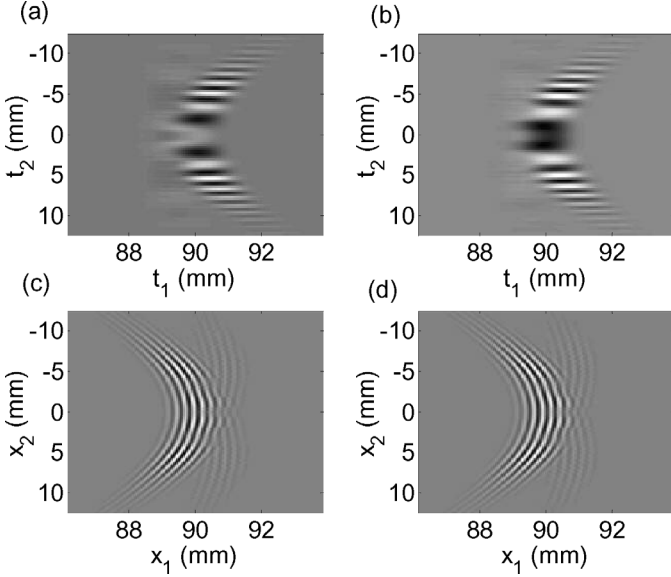


Fig. 3. Normalized in-phase and quadrature point-spread (a)–(b), and spatial sensitivity (c)–(d) functions for the array transducer described in Fig. 2. Images of I and Q psfs represent spread from a scatterer at a distance of 90 mm (far field). Similarly, I and Q spatial sensitivity functions are shown for pulse-echo temporal intervals corresponding to 90 mm, which is half the pulse-echo path distance.

speckle depend only on the overall shape of the pulse envelope [1], [2] and is independent of phase information. To extend this statistical analysis outside of the focal zone, (12) suggests that the precise phase of h or $[h_I, h_Q]$ is required to accurately model the statistical moments of the echo data g . Statistical analysis of echoes throughout the field is the main application of this linear systems analysis.

V. B-MODE SIGNALS

B-mode imaging systems display the envelope of the RF echo signal obtained from the magnitude of the $[I, Q]$ data:

$$g_e(\mathbf{t}) = \sqrt{g_I^2(\mathbf{t}) + g_Q^2(\mathbf{t})}, \quad (16)$$

or equivalently the magnitude of the analytic signal. Envelope detection is inherently nonlinear, thus linear systems analysis of ultrasound systems must be applied to either the RF or $[I, Q]$ data. The envelope of h , which we denote $h_e(\mathbf{x}, \mathbf{t})$, is important for modeling focal-region statistics of the B-mode image signals [1], [2], and may be written as $h_e = |h_o| = \sqrt{h_I^2 + h_Q^2} = \sqrt{h^2 + \tilde{h}^2}$. Because B-mode processing discards phase information, it is natural to wonder whether envelope detection is the optimal strategy for data visualization and, if not, what is the optimal strategy? Current research aims to address this question in the context of image quality assessment literature [5].

VI. THE LOCAL SHIFT INVARIANCE APPROXIMATION

As shown in Appendix A, 2-D image reconstruction maps the temporal coordinates of the echo data $g(t_1, t_2)$ into spatial coordinates associated with image pixels, $\hat{\gamma}(x_1, x_2)$. Furthermore, the spatiotemporal coordinate transformation is linear, $\mathbf{t} = \mathbf{B}\mathbf{x}$ and, therefore, interesting relationships exist between point-spread and spatial sensitivity functions when linear shift-invariance (LSIV) holds.

If we find that

$$h(\mathbf{x}, \mathbf{t}) \cong h(\mathbf{x} + \Delta\mathbf{x}, \mathbf{t} + \mathbf{B}\Delta\mathbf{x}) \quad (17)$$

over some range of $\Delta\mathbf{x}$, then we say that h is locally LSIV for values of \mathbf{x} where (17) holds. This region is often labeled isoplanetic. For such regions, h may be written as a function of one vector variable:

$$h(\mathbf{x}, \mathbf{t}) = h(\mathbf{t} - \mathbf{B}\mathbf{x}), \quad (18)$$

thus,

$$\begin{aligned} \text{ssf}(\mathbf{x}) &= h(\mathbf{t}_o - \mathbf{B}\mathbf{x} \mid \mathbf{t}_o) \Big|_{\mathbf{t}_o = \mathbf{B}\mathbf{x}_o} \\ &= h(-[\mathbf{B}(\mathbf{x} - \mathbf{x}_o)] \mid \mathbf{x}_o) \\ &= \text{psf}(-(\mathbf{t} - \mathbf{t}_o)). \end{aligned} \quad (19)$$

This means that the ssf, a function of \mathbf{x} , is a copy of the psf time-reversed about the point $\mathbf{t}_o = \mathbf{B}\mathbf{x}_o$. This is why there appears to be reflective symmetry between the psfs and ssfs shown in Fig. 2.

Eq. (19) is not valid and the system is not locally LSIV when amplitude profiles or wavefront curvatures vary significantly with position, as is the situation for strongly focused transducers. Fig. 4 shows farfield ssf and time-reversed psf A-scan lines Fig. 4(a) on axis and Fig. 4(b) 7.6 mm off axis. The phase mismatch off axis may be explained by the changing curvature of the wavefront over an assumed isoplanetic patch. The approximation is much better on axis [Fig. 4(a)] or in the focal region, where wavefront curvature is minimal.

In an isoplanetic region, the shape of the point-spread or spatial sensitivity functions do not change. One way of assessing the approximate size of an isoplanetic patch is to plot the normalized correlation coefficient between different sensitivity or point-spread functions as a function of temporal or spatial separation. Because it is often easier to compute the psf rather than the ssf, we choose to assess how the psf changes as a function of distance. More precisely, let $p_1(\mathbf{t}) = h(\mathbf{t}_1 \mid \mathbf{x})$ and $p_2(\mathbf{t}) = h(\mathbf{t} \mid \mathbf{x}_2 = \mathbf{x}_1 + \Delta\mathbf{x})$ be point-spread functions for spatial (object-space) points \mathbf{x}_1 and \mathbf{x}_2 . Then the normalized correlation coefficient for assessing shift invariance is:

$$C_{p_1 p_2}(\Delta\mathbf{x}) \equiv \frac{\int p_1(\mathbf{t}) p_2(\mathbf{t} - \mathbf{B}\Delta\mathbf{x}) dt}{\int p_1(\mathbf{t}) dt \int p_2(\mathbf{t}) dt} \quad (20)$$

$C_{p_1 p_2}(\Delta\mathbf{x})$ is a measure of the similarity between overlaid point-spread functions. By plotting $C_{p_1 p_2}(\Delta\mathbf{x})$ as a function of lag $\Delta\mathbf{x}$, the degree of shift invariance can

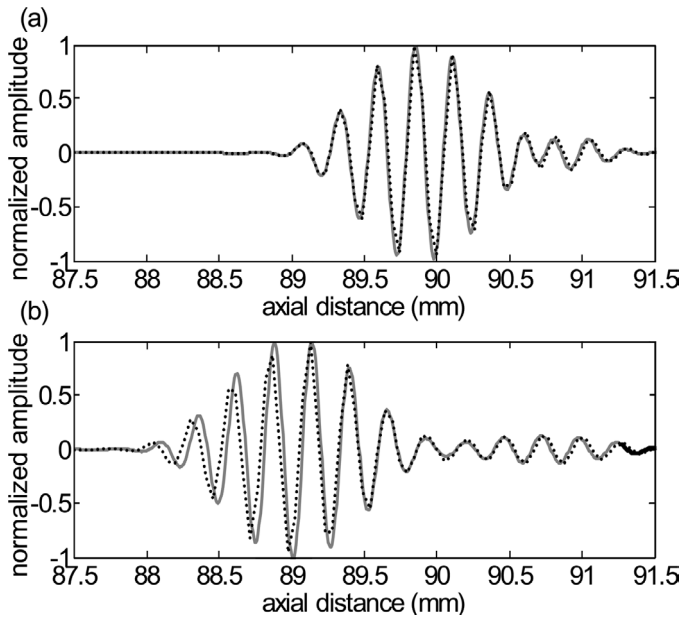


Fig. 4. Normalized farfield ssf and time-reversed psf A-scan lines (a) on axis and (b) 7.6 mm off axis. The parameters were the same as in Fig. 3.

be assessed. When $C_{p_1 p_2}(\Delta \mathbf{x})$ falls below a threshold value (e.g., 90%) we say that shift invariance fails. The suprathreshold region defines the extent of the isoplanetic patch. To relate the point-spread and spatial sensitivity functions as in (19), the temporal shape of the point-spread functions should not change as the scatterer location is moved spatially over the extent of the scattering volume associated with a given instant of time. Alternatively, the size of the isoplanetic patch should be larger than the temporal extent of the point-spread function itself, as seen in Fig. 5. The LSIV approximation holds across lateral scan lines for linear arrays, except when the beam is electronically steered or near the margins in which the aperture is reduced. The isoplanetic regions will be small along the beam axis for fixed-focus sources in which the wavefront curvature varies. Outside the focal region, highly curved, extensive ssf wavefronts may exhibit enough axial spatial extent to exceed the size of an isoplanetic patch. In this case, (19) does not hold and the symmetry between ssf and psf is lost. The 90% threshold isoplanetic patch for the farfield psf of Figs. 2(c) and (f), extended from 88.8 to 91.3 mm. Significant energy exists beyond this region; hence the lack of symmetry between the psf and ssf as seen in Fig. 4. Systems with dynamic focusing and aperture growth, as well as systems that use synthetic aperture approaches may be expected to have fairly large isoplanetic regions.

The local LSIV of isoplanetic regions fails for in-phase and quadrature signals. As is evident in Fig. 3, the I and Q ssfs are not approximated by time reversed I and Q psfs. However, the I and Q ssfs can be represented as a phase-shifted version of the RF ssf—or the time-reversed RF psf. Multiplying the phase factor $\exp(-i\omega_0 t)$ and the analytic ssf signal (approximated by the time-reversed psf

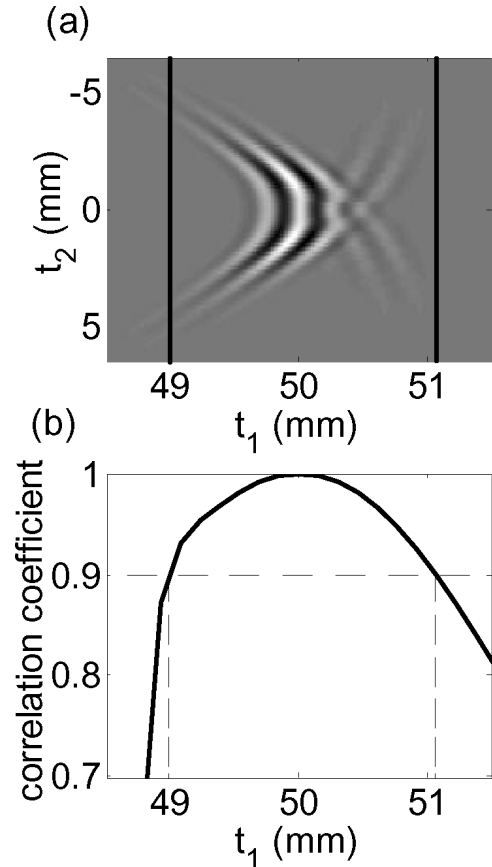


Fig. 5. A way to assess the size of an isoplanetic patch. The lines in (a) represent the point at which the correlation coefficient as defined by (20) reach 90% threshold. In this example, because most of the energy is contained within this region, the local LSIV approximation may be expected to be a good one. Point target was at 50 mm, and focal region was 60 mm. A two-cycle excitation was used, and the aperture's electromechanical impulse response was simulated as a two-cycle Hanning-windowed pulse. Otherwise, simulation parameters were the same as in Fig. 2.

whose argument has been converted to a spatial coordinate) $h(\mathbf{x} | t) + i\hat{h}(\mathbf{x} | t)$ and taking the real part of the result, the in-phase ssf may be obtained. The quadrature ssf may be obtained by taking the imaginary part of the product. Thus, with a local shift-invariance approximation, the RF point-spread functions may be used to compute statistical moments of the in-phase and quadrature signals without computing sensitivity functions. This may be useful when it is more natural to calculate psfs than ssfs, as is the case with many simulation packages.

When an isoplanetic region is larger than the sensitivity function, the LSIV approximation holds and (1) reduces to a convolution, e.g., $\bar{g}(\mathbf{x}) = [h * \gamma](\mathbf{x})$. The LSIV assumption allows us to express g and $\bar{g} = \langle g \rangle_n$ as functions of either \mathbf{x} or \mathbf{t} . Specifically, $g(\mathbf{t}(\mathbf{x})) = g(\mathbf{B}\mathbf{x})$. Under the isoplanetic assumption, our results reduce to those of Jensen [13, equation 45]. Walker and Trahey [14] chose to represent the LSIV imaging equation in frequency or k -space. In the Fraunhofer regime, this has a particularly elegant interpretation as the field profile is simply the Fourier transform of the aperture.

Although the validity of the local LSIV assumption for the RF signal is largely restricted to the focal region of array transducers, the assumption nevertheless is useful for analysis and interpretation. Let us define \check{h} as the pulse-echo impulse response, neglecting the quadratic frequency dependence of scattering [i.e., \check{h} is the LSIV approximation to the quantity in curly brackets in (9)]. This approximation allows the noise-averaged linear system to be written in the spatial frequency domain as [26]:

$$\begin{aligned}\bar{G}(\mathbf{k}) &= \mathfrak{S}_{\mathbf{x}} \{ \bar{g}(\mathbf{x}) \} = H(\mathbf{k})\Gamma(\mathbf{k}) \\ &= k_1^2 \check{H}(\mathbf{k})\Gamma(\mathbf{k}) = \check{H}(\mathbf{k})\Phi(\mathbf{k}),\end{aligned}\quad (21)$$

where $\mathbf{k} = (k_1, k_2, k_3)$ is the spatial angular-frequency vector (conjugate to \mathbf{x}), and H , \check{H} , and Γ are the spatial Fourier transforms of h , \check{h} , and γ , respectively. The scattering amplitude is defined as:

$$\Phi(\mathbf{k}) = -\frac{1}{4\pi} k_1^2 \Gamma(\mathbf{k}) = \frac{1}{2\pi z_o} \mathfrak{S}_{\mathbf{x}} \left\{ \frac{\partial^2 z(\mathbf{x})}{\partial x_1^2} \right\}, \quad (22)$$

where x_1 is the component of \mathbf{x} normal to the transducer surface as in Fig. 1. A local plane wave approximation is required to write (21) and (22), and hence its validity is restricted, in practice, to the focal region of ultrasound B-scans. The noise-averaged echo signal can now be written as [26], [27]:

$$\bar{g}(\mathbf{x}) = -2 \left[\check{h} * \frac{\partial^2}{\partial x_1^2} \left(\frac{z}{z_o} \right) \right] (\mathbf{x}) = -2 \left[h * \left(\frac{z}{z_o} \right) \right] (\mathbf{x}). \quad (23)$$

The first equality in (23) illustrates that sound is scattered whenever the second derivative of the relative acoustic impedance (in the direction of transmission) is nonzero. The second equality allows one to consider the acoustic impedance itself as the object function. The spatiotemporal impulse response function, h , thus acts as a spatial frequency filter on the object function $z(\mathbf{x})$. The spatial frequency response of this filter is described by H , which is the k -space picture of h [14]. Insana and Cook [28] give a useful LSIV approximation for a beam using a Gaussian signal model. They show that h acts as a bandpass filter of $z(\mathbf{x})$ in the axial direction, and as a lowpass filter of $z(\mathbf{x})$ in the lateral direction. The bandpass nature of h in the scanning direction is due to modulation about a carrier frequency, and the lowpass character in the lateral direction is due to the (unmodulated) taper of the beam profile.

VII. SIGNAL STATISTICS

The linear systems framework developed here and by others provides a starting point for analysis of signal statistics. Eq. (12) illustrates one way to compute the covariance of the RF signal. With a local isoplanetic assumption, the point-spread function can be used instead of the spatial

sensitivity, and our results match those of Walker and Trahey [14], with one important exception. They predicted that wavefront curvature played no role in the RF signal covariance between two signals when the respective apertures are coplanar. Their conclusion was based on stringent assumptions, including the Fraunhofer approximation and an assumption that phase curvature has no lateral positional dependence over some region of interest that does not extend too far off axis. Explicitly, for spatial positions \mathbf{x} far from the aperture $x_1 \gg \frac{k|\mathbf{r}|_{\max}^2}{2}$ and not too far off axis, so that $\cos(\mathbf{x}_1, \mathbf{r}-\mathbf{x}) \cong 1$, the continuous wave (CW) Fresnel approximation of (4) due to a sinusoidal excitation:

$$\begin{aligned}A(\mathbf{x}, k) &= \frac{\exp(ikx_1)}{i\lambda x_1} \exp \left[i \frac{k}{2x_1} (x_2^2 + x_3^2) \right] \\ &\int_{-\infty}^{\infty} \int_{-\infty}^{\infty} \left\{ \xi(\mathbf{r}) \exp \left[i \frac{k}{2x_1} |\mathbf{r}|^2 \right] \right\} \exp \left[-i \frac{2\pi}{\lambda x_1} (\mathbf{x} \cdot \mathbf{r}) \right] dS,\end{aligned}\quad (24)$$

reduces to the Fraunhofer approximation [21]:

$$\begin{aligned}A(\mathbf{x}, k) &= \frac{\exp(ikx_1)}{i\lambda x_1} \exp \left[i \frac{k}{2x_1} (x_2^2 + x_3^2) \right] \\ &\int_{-\infty}^{\infty} \int_{-\infty}^{\infty} \xi(\mathbf{r}) \exp \left[-i \frac{2\pi}{\lambda x_1} (\mathbf{x} \cdot \mathbf{r}) \right] dS.\end{aligned}\quad (25)$$

This is because the quadratic phase term $\exp \left[i \frac{k}{2x_1} |\mathbf{r}|^2 \right]$ in the Fresnel expression is approximately unity over unfocused aperture faces for points x_1 far enough away. When a focused aperture is used, the apodization ξ may be considered a complex quantity. Its purpose is to negate the $\exp \left[i \frac{k}{2x_1} |\mathbf{r}|^2 \right]$ phase term in the Fresnel integral and, hence, simulate the Fraunhofer region at a much closer range. The quadratic phase argument will be negligible in some depth of field about the focus of a focused transducer. In pre- or postfocal regions, where x_1 is comparable to or less than $\frac{k|\mathbf{r}|_{\max}^2}{2}$, however, the phase may be significant and the Fraunhofer approximation may fail. In these situations, phase curvature is dependent on lateral position, and the approximations of Walker and Trahey [14] do not hold. Their conclusion is, for example, applicable to the focal region of focused transducers in which wavefront curvature is essentially flat and farfield regions of unfocused transducers (as long as energy is concentrated in a region not too far off axis).

We give an example of how wavefront curvature can play a very important role in predicting speckle texture for focused transducers in pre- and postfocal regions. Consider an electronically swept linear array system with fixed focus and shift invariance in the lateral direction. We are interested in the correlation lengths of speckle along lateral scan lines. In this case the covariance (12) depends only on the difference $(\mathbf{t}-\mathbf{t}')$, and thus is simply a cross correlation. Eq. (12) tells us that, to compute the speckle cross correlation, one should slide the sensitivity map laterally, then multiply with a copy of itself, and integrate.

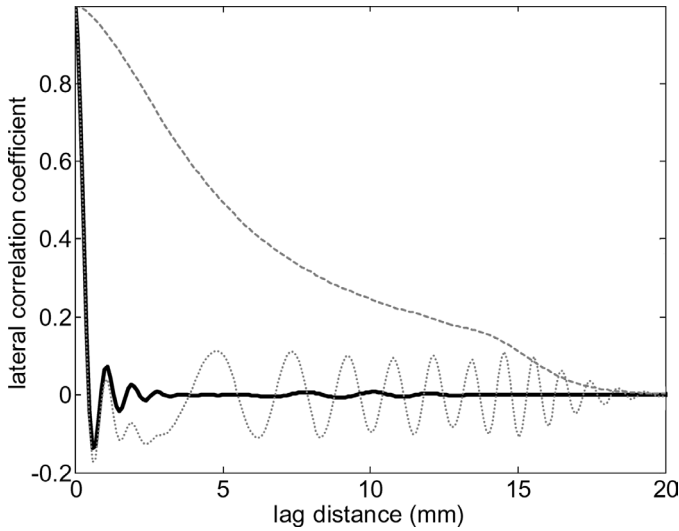


Fig. 6. Predicted correct and erroneous correlation coefficients of in-phase image data from lateral scan lines at 30 mm axial depth for a transducer with focus at 60 mm. Simulation parameters were otherwise the same as in Fig. 2. Solid line: the predicted true correlation coefficient using the spatial sensitivity functions. Dashed line: an erroneous predicted lateral correlation coefficient arrived at by ignoring phase oscillations. Dotted line: the erroneous lateral correlation coefficient arrived at by using the in-phase point-spread functions rather than in-phase sensitivity functions. The true nearfield speckle is predicted to be very narrow in the lateral direction due to wavefront curvature. Not shown is the in-phase correlation coefficient predicted by a phase-shifted, time-reversed RF psf. It differed from the correct lateral correlation coefficient by less than 1%.

In the near- and farfield, wavefront curvature is significant, and this procedure of shifting and multiplying will result in complex phase interference patterns that will quickly integrate to zero. Fig. 6 shows the predicted correlation lengths of in-phase speckle texture in the lateral direction for curved and flat wavefront sensitivity functions along with the corresponding erroneous predictions that use in-phase psfs instead of ssfs, and neglect phase or assume a flat wavefront field of equal shape and scattering volume. Speckle patterns corresponding to the curved wavefront field decorrelate more quickly than does the flat wavefront field. This is one reason why speckle texture appears fine in the near and farfield regions of ultrasound B-scans even though the pulse energy is spread out very broadly. A related connection to the literature concerns phase aberration. Speckle has been observed to be broadest whenever aberrations are least [29], [30]. Phase aberrations cause irregularities in phase fronts that induce rapid decorrelation even though the pulse volumes are very large.

The isoplanetic approximation to the lateral correlation coefficient of Fig. 6 (not shown) for lateral speckle correlation is very good (less than 1% maximum deviation) because lateral shift invariance is assumed. Fig. 7 shows correlations in the axial direction, and the corresponding isoplanetic approximation. In the axial case the isoplanetic assumption deviates significantly (almost 20% at 1-mm lag) from the full shift-variant computation. Better agreement may be expected for shorter pulses because

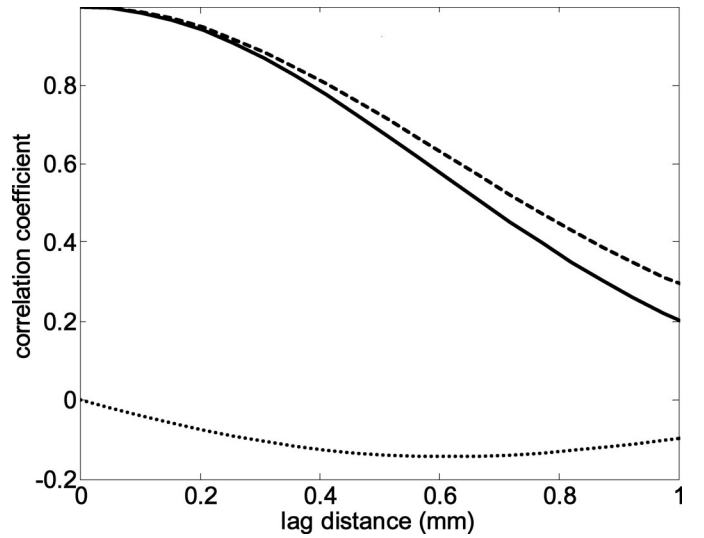


Fig. 7. Normalized covariances $K_{II}(t, t + \Delta t)$, solid and dashed lines, and $K_{IQ}(t, t + \Delta t)$, dotted line, of in-phase and quadrature signals along axial scan lines as a function of lag distance $\Delta x = c\Delta t/2$. Calculations were based on 2-D field distributions from a focused array transducer with focus at 6 cm, and $ct/2 = 90$ mm. Otherwise, parameters were the same as in Fig. 2. The dashed line represents the computation using the isoplanetic approximation (modeling I and Q ssfs by time-reversed, phase-shifted psfs). The solid line is the computation with the full shift-variant theory. Note from the dotted line that in-phase and quadrature correlations exist. This may be explained as coupling between direct and edge waves, as shown in Fig. 9.

the axial correlation distance will be shorter relative to the size of the isoplanetic patch. For simplicity, in all the examples shown, we imagine that we are imaging a 2-D planar distribution of scatterers, so that we can assume the ssf is a 2-D instead of a 3-D function.

If the system is locally shift invariant, and the object can be modeled by a zero mean wide sense stationary (WSS) random process, then the covariance matrices are completely characterized by autocorrelation functions. In the continuous sampling limit, the eigenvalues of the covariance matrix are simply the power spectrum. Thus,

$$K(\mathbf{x}_1, \mathbf{x}_1 + \Delta\mathbf{x}) = R(\Delta\mathbf{x}) = h(\Delta\mathbf{x}) * R_\gamma(\Delta\mathbf{x}) * h(-\Delta\mathbf{x}) + R_n(\Delta\mathbf{x}) \longleftrightarrow_{\mathfrak{F}} |H(\mathbf{k})|^2 S_\gamma(\mathbf{k}) + \text{NPS}(\mathbf{k}), \quad (26)$$

where $R_\gamma(\Delta\mathbf{x})$ and $S_\gamma(\mathbf{k})$ are the autocorrelation and power-spectral representations of the object function, respectively, and $R_n(\Delta\mathbf{x})$ and $\text{NPS}(\mathbf{k})$ are the autocorrelation and power spectrum of the noise, respectively.

One curiosity is that the covariance itself depends on wavefront curvature, yet from (26), only the magnitude of $H(\mathbf{k})$ has a role in speckle properties. The conclusion is that curved wavefront ssfs have spatial phase curvature information in $|H(\mathbf{k})|$.

Intriguingly, the lateral spatial frequency bandwidth [Fig. 8(d)] of the large curved wavefront sensitivity in Fig. 8(c) is broader than the bandwidth [Fig. 8(b)] of the smaller focal region sensitivity of Fig. 8(a). Specifically,

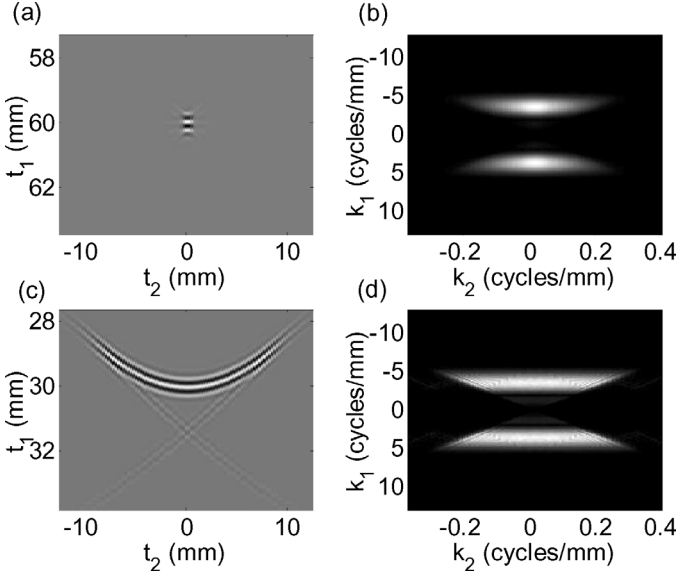


Fig. 8. (a) Focal and (c) nearfield RF psfs due to a 3 MHz fixed focus linear array of height 0.5 cm, with 64 active elements of width λ separated by distances of 0.1 mm. Azimuthal focus was 6 cm. The beam was electronically swept laterally across the point target located at (a) 6 cm and (c) 3 cm. (b) and (d) are the k-space representations of (a) and (c), respectively. A two-cycle excitation was used, and the aperture’s electromechanical impulse response was simulated as a two-cycle Hanning-windowed pulse.

the effective lateral bandwidth of Fig. 8(d) as defined by Bendat and Piersol [31], and evaluated at the axial frequency maximum was 74% broader than that of Fig. 8(b). Thus, from an information-theoretic point of view, the curved wavefront ssf has potentially more spatial resolution available, even though the pulse volume is considerably larger! This can be better understood by realizing that a slice through the sensitivity function in the lateral direction looks like a chirp function. A matched or mismatched compression filter could potentially be applied to regain spatial resolution while improving signal to noise, similar to current coded excitation schemes [32]. A fascinating possibility for designing ultrasound systems could be the introduction of an engineered, coded excitation in the lateral direction of the beam, similar to work that has been done for 2-D velocity estimation using array transducers [33], [34].

As a final illustration of the application of this work, we give an example of how shift-variant systems may exhibit statistical coupling of in-phase and quadrature signals along axial scan lines. Most current literature assumes independence of I and Q channels. It is well-known that the on-axis acoustic response consists of direct and edge waves, and that these contributions will have a position-dependent phase delay. Keeping this in mind, now consider computing the covariance between in-phase and quadrature signals at various points of time. Eq. (12) tells us that we should multiply sensitivity functions for the I and Q signals then integrate. This integration will not tend to zero if portions of the in-phase signal are not exactly 90° out of phase with the quadrature, as demonstrated in

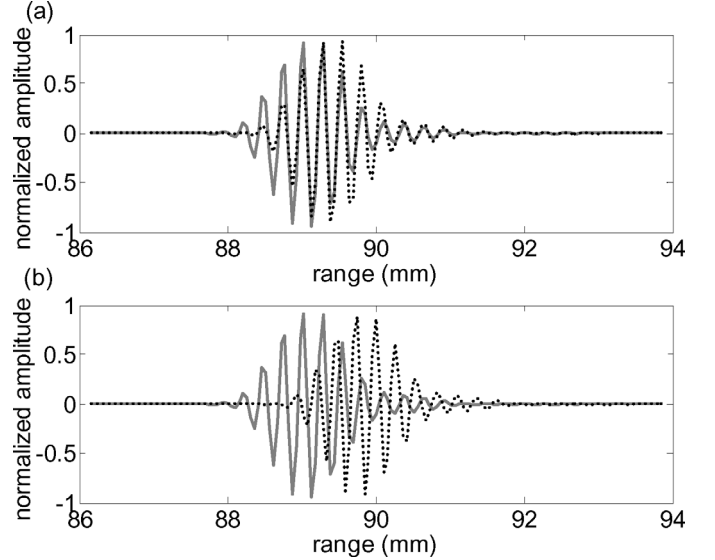


Fig. 9. (a) Axial slices through in-phase ssfs. This is to illustrate that in-phase ssfs are always in phase with each other, even though the envelope may shift. (b) In-phase (solid line) and quadrature (dotted line) ssfs are not 90° out of phase. At about the 90-mm point, the direct wave of the quadrature ssf is almost 180° out of phase with the edge wave of the in-phase ssf.

Fig. 9. Statistical independence between I and Q signals can be expected in the focal zone of unapodized transducers as direct and edge waves are approximately superimposed with a constant phase relationship. Understanding these edge-wave effects may be important for understanding or eliminating unwanted image correlations, both from a system design point of view and an image processing perspective. The degree of statistical dependence between I and Q channels will be diminished greatly with decreasing edge-wave amplitudes. Consequently, apodization may significantly reduce edge wave amplitudes and abate $I - Q$ correlation.

VIII. CONCLUSIONS

A linear systems framework based on a solution to the wave equation for inhomogeneous media has been presented that is similar to others [11]–[13]. With certain approximations, our results reduce to a continuum extension of the Tupholme-Stepanishen theory [6]–[10]. Although their focus has been on point-spread functions, ours is on spatial sensitivity functions. For each echo sample, the spatial sensitivity function reveals the sensitivity of the ultrasound system to each location in the object. These functions, along with their in-phase and quadrature counterparts are important in the computation of statistical moments. When local shift-invariance holds (as is the case near the focal region of an array transducer), the spatial sensitivity functions are shown to be similar to point-spread functions, which are time reversed about the axial position of the scatterer location. This time-reversal property does not apply to the in-phase and quadrature distri-

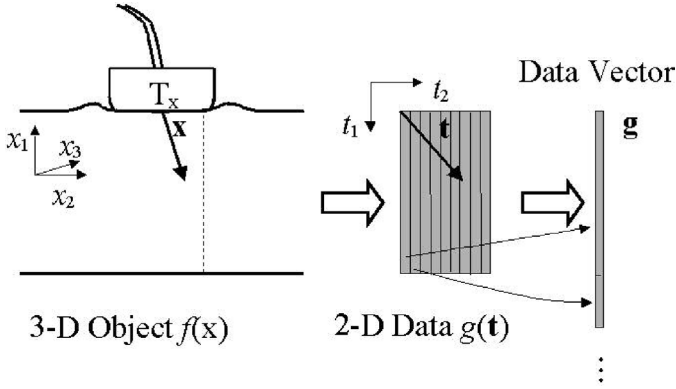


Fig. 10. Illustration of geometries for the object and data vectors using a linear array transducer.

butions. The LSIV approximation together with a plane-wave approximation has further been used to understand the system response as a spatial frequency bandpass filter of acoustic impedance $z(\mathbf{x})$ in the axial direction, and as a lowpass filter of $z(\mathbf{x})$ in the lateral direction. An equivalent interpretation suggests that ultrasound systems are sensitive only to the second derivative of $z(\mathbf{x})$ with respect to the scanning direction. In situations in which local shift invariance does not apply, the full shift-variant theory must be used. Shift-variant, in-phase and quadrature spatial sensitivity functions may be particularly important for the evaluation of statistical properties of demodulated or envelope-detected images of realistic ultrasound imaging systems. Such statistical characterization may be useful for quantifying image quality and for design of image processing algorithms. Our theory predicts that wavefront curvature and phase information contained within sensitivity functions is essential for explaining the complex speckle structure apparent in ultrasound images. Coupling between direct and edge waves introduces statistical correlations between I and Q channels. Also revealed is an opportunity to enhance near- and far-field spatial resolution by matched filtering unfocused beams. Ultimately this work will aid our understanding of fundamental performance limits, optimum image processing strategies, and quantitative image quality metrics for ultrasonography.

APPENDIX A

This appendix provides examples of object, data, and image function representations that may be useful in several ultrasonic applications of the linear imaging equation (1).

One common data structure for B-mode acquisition is shown in Fig. 10. A linear array generates beamformed echo sequences oriented in columns with elements $g(\mathbf{t}) = g(t_1, t_2) = g(\ell T, mLT)$. The L range samples are placed in columns corresponding to each A-line and assigned a discrete time stamp $t_1 = \ell T$, where $0 \leq \ell \leq L - 1$ are integers and T is the temporal sampling interval. Columns are filled left to right with sequenced A-line recordings,

where $t_2 = mLT$, $0 \leq m \leq M - 1$. The acquisition time is given by $t' = t_1 + t_2 = (\ell + mL)T$, and the integer ℓ is indexed completely between 0 and $L - 1$ before m is incremented. In this example, sequentially acquired data are represented by a 2-D matrix of echo samples $g[\ell, m]$. It is often convenient to organize all the data from a scan-plane into a single LM -dimensional column vector \mathbf{g} with elements $g[\ell + mL]$. Then from (1) we can write the imaging equation as a continuous-to-discrete transformation:

$$\mathbf{g} = \int d\mathbf{x} h(\mathbf{x}, t'[\ell, m])\gamma(\mathbf{x}) + \mathbf{n} = \mathcal{H}\{\gamma(\mathbf{x})\} + \mathbf{n}, \quad (\text{A1})$$

where \mathcal{H} in the last form is a linear operator on γ that generates \mathbf{g} .

To facilitate diagnostic interpretation, human observers require that echo locations be one-to-one with the corresponding object locations. Consequently, we apply a discrete-to-discrete reconstruction operator \mathcal{O} , viz., $\hat{\gamma} = \mathcal{O}\{\mathbf{g}\}$, that converts echo data into an image of the object, $\hat{\gamma}$. Like \mathbf{g} , $\hat{\gamma}$ is a vector of length LM . If \mathcal{O} is linear, then [3]:

$$\begin{aligned} \hat{\gamma} &= \mathcal{O}\mathcal{H}\{\gamma(\mathbf{x})\} + \mathcal{O}\{\mathbf{n}\} \\ &= \mathcal{S}\{\gamma(\mathbf{x})\} + (\mathcal{O}\mathcal{H} - \mathcal{S})\{\gamma(\mathbf{x})\} + \mathcal{O}\{\mathbf{n}\}. \end{aligned} \quad (\text{A2})$$

where \mathcal{S} is the sampling operator. The first term on the right side is the sampled object, the second term is the bias between the reconstructed image and sampled object, and the third term is the image noise. If the task is to obtain an image of the object nearest its true form, a superior linear imaging system minimizes the second and third terms. B-mode image reconstruction is nonlinear, so (A2) does not apply. Nevertheless B-mode image reconstruction is straightforward. Essentially we take the envelope of the echo data, [see (16)] and convert temporal coordinates to spatial coordinates: $t_1 = \ell T \rightarrow \ell cT/2 = \ell \Delta X_1$, and $t_2 = mLT \rightarrow m \Delta X_2$, where c is the speed of sound and ΔX_1 and ΔX_2 are the vertical and horizontal pixel dimensions corresponding to the axial and lateral (pitch) spatial sampling intervals. As part of the reconstruction process, we normally convert the temporal axes of the data into spatial axes via the inverse of the coordinate transformation $\mathbf{t} = \mathbf{B}\mathbf{x}$, where, in the case of swept-scan 3-D B-mode imaging, \mathbf{B} is a diagonal matrix. Specifically, the mapping is:

$$\begin{bmatrix} t_1 \\ t_2 \\ t_3 \end{bmatrix} = \begin{bmatrix} 2/c & 0 \\ T/\Delta X_2 & \\ 0 & T/\Delta X_3 \end{bmatrix} \begin{bmatrix} x_1 \\ x_2 \\ x_3 \end{bmatrix}. \quad (\text{A3})$$

To consider other ultrasonic techniques requires that we expand the dimension of the time vector \mathbf{t} . Doppler estimates use several A-line acquisitions at each lateral transducer position. Fast-time (range) samples, identified above by the index ℓ , are repeatedly acquired Q times before indexing m to form a slow-time data set at times $t_0 = qLT$ [35]. The integer index is $0 \leq q \leq Q - 1$,

and we assume the temporal pulse-repetition interval is $T_p = LT$. Further, to add data for either 3-D, B-mode imaging or strain imaging, sequential scan planes are acquired at times $t_3 = rMQLT$, where $0 \leq r \leq R - 1$ and the temporal frame-acquisition interval $T_s = QMLT$. For 3-D imaging, r corresponds to a spatial index ΔX_3 , but for strain imaging a fixed-object region is scanned ($\Delta X_3 = 0$). The indices are nested as follows: $g(\mathbf{t}) = g(t_1, t_0, t_2, t_3) = g(\ell T, qLT, mQLT, rMQLT)$, and the acquisition time is $t' = t_1 + t_0 + t_2 + t_3 = (\ell + (q + (m + rM)Q)L)T$. Of course, the reconstruction operator \mathcal{O} and coordinate transformation matrix \mathbf{B} will change depending on the technique, but \mathcal{O} is nonlinear for all the techniques described above.

With the above data structure, it is easy to allow the object function to change with time. This situation occurs with blood flow and tissue deformation. The object function assumes the form $\gamma(\mathbf{x}, t'[\ell, q, m, r])$, therefore,

$$g[\ell, q, m, r] = \int d\mathbf{x} h(\mathbf{x}, t') \gamma(\mathbf{x}, t') + n[\ell, q, m, r]. \quad (\text{A4})$$

Re-mapping the four-dimensional matrix into a vector gives the compact form similar to (A1):

$$\mathbf{g} = \mathcal{H} \{ \gamma(\mathbf{x}, t') \} + \mathbf{n}. \quad (\text{A5})$$

Although objects and images are naturally functions of space and time, we believe it is easier to consider echo data acquired serially strictly as a function of time. Yet, by creating a time vector, data can be conveniently partitioned into segments that intuitively correspond to spatial and temporal coordinates of the reconstructed image.

APPENDIX B

Here we summarize the derivation of (3). From (2), the homogeneous wave equation in inhomogeneous media, multiply by -1 and add:

$$\frac{1}{\rho_o(\mathbf{x})} \nabla^2 p - \kappa_o \frac{\partial^2 p}{\partial t^2}.$$

Then multiply by ρ_o to find

$$\nabla^2 p(\mathbf{x}, t) - \frac{1}{c^2} \frac{\partial^2 p(\mathbf{x}, t)}{\partial t^2} = \frac{\gamma_\kappa(\mathbf{x})}{c^2} \frac{\partial^2 p(\mathbf{x}, t)}{\partial t^2} + \nabla \cdot (\gamma_p(\mathbf{x}) \nabla p(\mathbf{x}, t)), \quad (\text{B1})$$

where $\gamma_\kappa(\mathbf{x}) = (\kappa(\mathbf{x}) - \kappa_o) / \kappa_o$, $\gamma_p(\mathbf{x}) = (\rho(\mathbf{x}) - \rho_o) / \rho(\mathbf{x})$, and $c^2 = 1 / \rho_o \kappa_o$. Using $p(\mathbf{x}, t) = p_\omega(\mathbf{x}) \exp(i\omega t)$, the following time-independent solution to (B1) is found.

$$\nabla^2 p_\omega(\mathbf{x}) - k^2 p_\omega(\mathbf{x}) = -q_\omega(\mathbf{x}), \quad (\text{B2})$$

where

$$q_\omega(\mathbf{x}) = k^2 \gamma_\kappa(\mathbf{x}) p_\omega(\mathbf{x}) - \nabla \cdot (\gamma_p(\mathbf{x}) \nabla p_\omega(\mathbf{x})). \quad (\text{B3})$$

Eq. (B2) is still a homogeneous wave equation as it has no sources or sinks. The terms on the right describe scattering sources that redirect energy but do not add or subtract from the total. A solution to (B2) can be found using the Green's function approach [18]. The total field is the sum of the incident and scattered fields:

$$p_\omega(\mathbf{x}) = p_{\omega_i}(\mathbf{x}) + p_{\omega_s}(\mathbf{x}), \quad (\text{B4})$$

where $p_{\omega_i}(\mathbf{x})$ is the incident pressure field and

$$p_{\omega_s}(\mathbf{r}) = \int_V d\mathbf{x} q_\omega(\mathbf{x}) G_\omega(\mathbf{r} | \mathbf{x}) \quad (\text{B5})$$

is the scattered field. The Green's function is defined as:

$$G_\omega(\mathbf{r} | \mathbf{x}) = \frac{1}{4\pi} \frac{\exp(-ik|\mathbf{r} - \mathbf{x}|)}{|\mathbf{r} - \mathbf{x}|} \quad (\text{B6})$$

From (B3) and (B5) we find the scattered field as:

$$\begin{aligned} p_{\omega_s}(\mathbf{r}) &= \int_V d\mathbf{x} \left\{ k^2 \gamma_\kappa(\mathbf{x}) p_\omega(\mathbf{x}) G_\omega(\mathbf{r} | \mathbf{x}) \right. \\ &\quad \left. - G_\omega(\mathbf{r} | \mathbf{x}) \nabla \cdot (\gamma_p(\mathbf{x}) \nabla p_\omega(\mathbf{x})) \right\} \\ &= \int_V d\mathbf{x} \left\{ k^2 \gamma_\kappa(\mathbf{x}) p_\omega(\mathbf{x}) G_\omega(\mathbf{r} | \mathbf{x}) \right. \\ &\quad \left. + \gamma_p(\mathbf{x}) [\nabla p_\omega(\mathbf{x}) \cdot \nabla G_\omega(\mathbf{r} | \mathbf{x})] \right\}. \end{aligned} \quad (\text{B7})$$

The last expression was obtained by using the product rule for differentiation followed by Gauss's theorem. This is the scattered pressure field at points on the receiving transducer surface. It is a function of the total field $p_\omega(\mathbf{x})$, which is well approximated by the incident field $p_{\omega_i}(\mathbf{x})$ under a weak-scattering hypothesis as is reasonable in biological tissue. From [17] the incident field from a quasiplanar surface is given as:

$$p_i(\mathbf{x}, t) = i\rho_o c k U(\omega) \exp(i\omega t) A(\mathbf{x}, t), \quad (\text{B8})$$

where A is the velocity potential described in (4). Integrating the scattered pressure (B7) over the transducer surface S , and applying the weak scattering approximation and (B8), the expression (3) for the force exerted on the transducer is obtained.

REFERENCES

- [1] R. F. Wagner, S. W. Smith, J. M. Sandrik, and H. Lopez, "Statistics of speckle in ultrasound B-scans," *IEEE Trans. Sonics Ultrason.*, vol. 30, pp. 156–163, May 1983.
- [2] R. F. Wagner, M. F. Insana, and D. G. Brown, "Statistical properties of radio-frequency and envelope-detected signals with applications to medical ultrasound," *J. Opt. Soc. Amer. A*, vol. 4, pp. 910–922, May 1987.
- [3] H. H. Barrett, "Objective assessment of image quality: Effects of quantum noise and object variability," *J. Opt. Soc. Amer. A*, vol. 7, pp. 1266–1278, July 1990.

- [4] H. H. Barrett, J. L. Denny, R. F. Wagner, and K. J. Meyers, "Objective assessment of image quality. II. Fisher information, Fourier crosstalk, and figures of merit for task performance," *J. Opt. Soc. Amer. A*, vol. 12, pp. 834–852, May 1995.
- [5] H. H. Barrett, C. K. Abbey, and E. Clarkson, "Objective assessment of image quality. III. ROC metrics, ideal observers, and likelihood-generating functions," *J. Opt. Soc. Amer. A*, vol. 15, pp. 1520–1535, June 1998.
- [6] G. E. Tupholme, "Generation of acoustic pulses by baffled plane pistons," *Mathematika*, vol. 16, pp. 209–224, 1969.
- [7] P. R. Stepanishen, "Acoustic transients from planar axisymmetric vibrators using the impulse response approach," *J. Acoust. Soc. Amer.*, vol. 70, pp. 1176–1181, Oct. 1981.
- [8] P. R. Stepanishen, "The time-dependent force and radiation impedance on a piston in a rigid infinite planar baffle," *J. Acoust. Soc. Amer.*, vol. 49, pp. 841–849, Mar. 1971.
- [9] P. R. Stepanishen, "Transient radiation from pistons in a infinite planar baffle," *J. Acoust. Soc. Amer.*, vol. 49, pp. 1627–1638, May 1971.
- [10] P. R. Stepanishen, "Pulsed transmit/receive response of ultrasonic piezoelectric transducers," *J. Acoust. Soc. Amer.*, vol. 69, pp. 1815–1827, June 1981.
- [11] J. C. Gore and S. Leeman, "Ultrasonic backscattering from human tissue: A realistic model," *Phys. Med. Biol.*, vol. 22, pp. 317–326, 1997.
- [12] M. Fatemi and A. C. Kak, "Ultrasonic B-scan imaging: Theory of image formation and a technique for restoration," *Ultrason. Imag.*, vol. 2, pp. 1–47, 1980.
- [13] J. A. Jensen, "A model for the propagation and scattering of ultrasound in tissue," *J. Acoust. Soc. Amer.*, vol. 89, pp. 182–190, Jan. 1991.
- [14] W. F. Walker and G. E. Trahey, "The application of K-space in Pulse Echo Ultrasound," *IEEE Trans. Ultrason., Ferroelect., Freq. Contr.*, vol. 45, pp. 541–558, May 1998.
- [15] W. F. Walker, "The significance of correlation in ultrasound signal processing," in *Proc. IEEE*, vol. 4325, Feb. 2001, pp. 159–171.
- [16] L. A. Chernov, *Wave Propagation in a Random Medium*. New York: McGraw-Hill, 1960.
- [17] L. E. Kinsler, A. R. Frey, A. B. Coppens, and J. V. Sanders, *Fundamentals of Acoustics, 4th ed.* New York: Wiley, 2000.
- [18] M. F. Insana and D. G. Brown, "Acoustic scattering theory applied to soft biological tissues," in *Ultrasonic Scattering in Biological Tissues*. K. K. Shung and G. A. Thieme, Eds. Boca Raton, FL: CRC Press, 1993, pp. 75–124.
- [19] P. M. Morse and K. U. Ingard, *Theoretical Acoustics*. New York: McGraw-Hill, 1968.
- [20] M. F. Insana, R. F. Wagner, D. G. Brown, and T. J. Hall, "Describing small-scale structure in random media using pulse-echo ultrasound," *J. Acoust. Soc. Amer.*, vol. 87, pp. 179–192, Jan. 1990.
- [21] J. W. Goodman, *Introduction to Fourier Optics, 2nd ed.* New York: McGraw-Hill, 1996.
- [22] M. Ueda and H. Ichikawa, "Analysis of an echo signal reflected from a weakly scattering volume by a discrete model of the medium," *J. Acoust. Soc. Amer.*, vol. 70, pp. 1768–1775, Dec. 1981.
- [23] P. T. Christopher and K. J. Parker, "New approaches to the linear propagation of acoustic fields," *J. Acoust. Soc. Amer.*, vol. 90, pp. 507–521, July 1991.
- [24] J. A. Jensen and N. B. Svendsen, "Calculation of pressure fields from arbitrarily shaped, apodized, and excited ultrasound transducers," *IEEE Trans. Ultrason., Ferroelect., Freq. Contr.*, vol. 39, pp. 262–267, Mar. 1992.
- [25] G. E. Tupholme, "Generation of an axisymmetrical acoustic pulse by a deformable sphere," *Proc. Cambridge Phil. Soc.*, vol. 63, pp. 1285–1308, 1967.
- [26] M. F. Insana, L. T. Cook, M. Bilgen, P. Chaturvedi, and Y. Zhu, "Maximum-likelihood approach to strain imaging using ultrasound," *J. Acoust. Soc. Amer.*, vol. 107, pp. 1421–1434, Mar. 2000.
- [27] F. Kallel, M. Bertrand, and J. Meunier, "Speckle motion artifact under tissue rotation," *IEEE Trans. Ultrason., Ferroelect., Freq. Contr.*, vol. 41, pp. 105–122, Jan. 1994.
- [28] M. F. Insana and L. T. Cook, "Bioelasticity Imaging: System Design," in *Proc. IEEE*, vol. 3659, pp. 224–235, Feb. 1999.
- [29] S. W. Flax and M. O'Donnell, "Phase-aberration corrections using signals from point reflectors and diffuse scatterers: Basic principles," *IEEE Trans. Ultrason., Ferroelect., Freq. Contr.*, vol. 35, pp. 758–767, Nov. 1988.
- [30] S. W. Smith, G. E. Trahey, S. M. Hubbard, and R. F. Wagner, "Properties of acoustical speckle in the presence of phase aberration. II. Correlation lengths (medical application)," *Ultrason. Imag.*, vol. 10, pp. 29–51, Jan. 1988.
- [31] J. S. Bendat and A. G. Piersol, *Random Data: Analysis and Measurement Procedures*. New York: Wiley-Interscience, 1971.
- [32] M. O'Donnell, "Coded excitation system for improving the penetration of real-time phased-array imaging systems," *IEEE Trans. Ultrason., Ferroelect., Freq. Contr.*, vol. 39, pp. 341–351, May 1992.
- [33] M. E. Anderson, "Multi-dimensional velocity estimation with ultrasound using spatial quadrature," *IEEE Trans. Ultrason., Ferroelect., Freq. Contr.*, vol. 45, pp. 852–861, May 1998.
- [34] J. A. Jensen and P. Munk, "A new method for estimation of velocity vectors," *IEEE Trans. Ultrason., Ferroelect., Freq. Contr.*, vol. 45, pp. 837–851, May 1998.
- [35] J. A. Jensen, *Estimation of Blood Velocities Using Ultrasound: A Signal Processing Approach*. New York: Cambridge Univ. Press, 1996.

Roger J. Zemp was born in Calgary, Alberta, Canada in 1974. He earned a B.Sc. in physics in 1998 from the University of Alberta in Edmonton, where he also worked at the Center for Subatomic Physics doing particle physics simulations. He spent a summer at the Defense Research Establishment Ottawa working as a research assistant in a pulsed-Doppler radar laboratory. In 2000 he completed a MS in Electrical and Computer Engineering at the Institute of Biomedical and Biomedical Engineering, University of Toronto, where he worked on modeling nonlinear propagation of ultrasound in tissue for harmonic imaging applications. He is currently a PhD candidate in the Department of Biomedical Engineering at the University of California, Davis. His dissertation is on information theoretic and experimental techniques for performance assessment of static and dynamic signals for cancer detection using ultrasound systems.

Craig K. Abbey is an assistant Professor of Biomedical Engineering at the University of California, Davis. His research is in the area of image analysis and evaluating the impact of imaging methodologies on diagnostic accuracy. He completed his doctoral work in 1998 under Prof. Harrison H. Barrett at the University of Arizona. He then spent two years as a research fellow at Cedars-Sinai Medical Center and one year as a postdoctoral fellow in Biophysics at UCLA with Prof. James S. Whiting.

Michael F. Insana received his PhD in medical physics from the University of Wisconsin–Madison in 1983. His dissertation topic was acoustic scattering and absorption in biological tissues. He was a research physicist at the FDA from 1984–1987, where he developed methods for describing tissue microstructure from the statistical properties of echo signals. From 1987–1999, he was with the Department of Radiology at the University of Kansas Medical Center. There he directed an imaging research lab that designed and evaluated new ultrasonic imaging methods for studying progressive renal failure and breast cancer. Since 1999, Mike has been Professor of Biomedical Engineering at the University of California, Davis. He is vice chair of the department and chair of the graduate group. His research is the development of novel ultrasonic instrumentation and methods for imaging soft tissue microstructure, elasticity and blood flow. The goal is to understand basic mechanisms of tumor formation and responses to therapy. His research includes the fundamentals of imaging system design and performance evaluation, signal processing, detection and estimation. He is a member of the IEEE and ASA, Fellow of the Institute of Physics, and Associate Editor for IEEE Transaction on Medical Imaging.